Journal of Marine Research, 53, 995–1024, 1995

Analysis of the barotropic model of the subtropical gyre in the ocean for finite Reynolds numbers. Part II.

by V. A. Sheremet[1,2], V. M. Kamenkovich[1,3] and A. R. Pastushkov[1]

ABSTRACT

This paper is a continuation of Part I of the suggested study of the barotropic model of the subtropical gyre for finite Reynolds numbers. The statement of the problem, the motivation of the analysis, and the description of the general properties of the solution are presented in Part I (Kamenkovich *et al.,* 1995). Here, in Part II of the study, the detailed investigations of the peculiarities of the solution are offered. The most striking feature of the solution is the formation of a recirculation gyre in the northwest corner of the basin. To study the gyre structure for various Reynolds numbers the time-averaged fields of the stream function, and that of the relative and potential vorticity are thoroughly examined. The role of the eddies, appeared within the boundary layer, in the transfer of positive vorticity from the west coast is clarified. The analysis of the energy characteristics of the system is presented and the vorticity balance both integral and regional (within a closed streamline) is elucidated. Finally, the consistent discussion of the process of the formation of the recirculation gyre for different Reynolds numbers is suggested.

1. Introduction

This is Part II of the presented analysis of the barotropic model of the subtropical gyre for finite Reynolds numbers R. The statement of the problem and motivation for its investigation was given in Part I of the analysis (Kamenkovich *et al.,* 1995; hereafter will be called KSPB) and will not be repeated here. In KSPB the general properties of the solution of the problem and the dependence of the solution on the value of the Reynolds number are described. The basic result of such a study is the proof of existence of two critical values of the Reynolds number R_C and R_L ($R_C = 0.38, R_L = 1.6$). Some evidence was presented that the steady boundary-layer-type solution of the problem is unstable for $R_C < R < R_L$ and does not exist at all for $R > R_L$. It was shown also that for finite R the permanent intensive recirculation gyre is formed. Two regimes in the evolution of the solution were identified: the spin-up and quasistationary regimes. During the quasistationary regime the periodic appear-

1. Laboratory of Geophysical Fluid Dynamics, P. P. Shirshov Institute of Oceanology, Russian Academy of Sciences, Krasikova St. 23, Moscow 117218, Russia.

2. Present address: Scripps Institution of Oceanography, La Jolla, California, 92093-0230, U.S.A.

3. Present address: Lamont-Doherty Earth Observatory of Columbia University, Palisades, New York 10964, U.S.A.

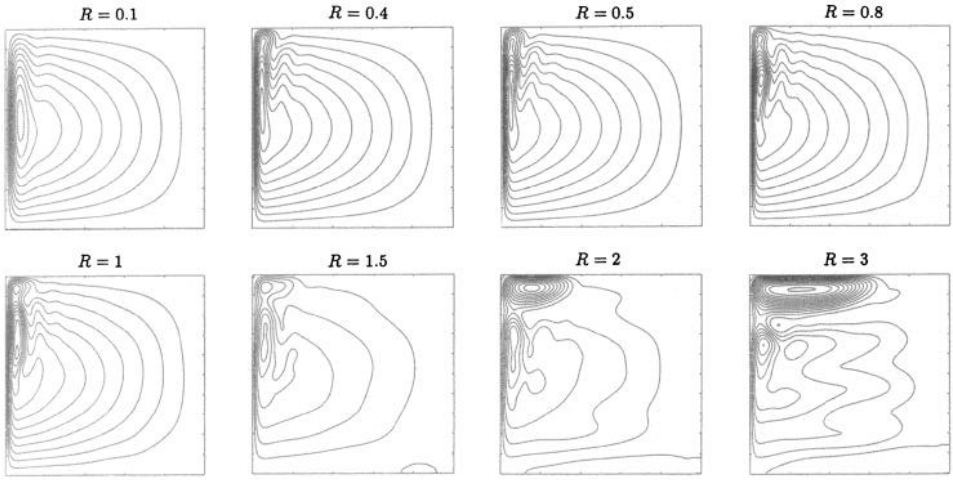

Figure 1. The isoline patterns of time-averaged stream function $\overline{\psi}$ for several Reynolds numbers: $R = 0.1; 0.4; 0.5; 0.8; 1; 1.5; 2; 3$. For $R < R_C \simeq 0.38$ the time averaged solutions are almost exactly the steady solutions. The contour interval, $CI = 0.1$ for $R = 0.1 - 1$; $CI = 0.2$ for $R = 1.5; 2; 3$.

ance of the northward moving eddies in the boundary layer was observed. The detailed analysis of the structure of these peculiarities of the solution and physical mechanisms responsible for their formation is highly needed to better understand the dynamics of the western boundary current. Such analysis is presented in this paper. In Section 2 the time-averaged fields of the stream function, of relative and potential vorticity are thoroughly examined. In Section 3 the characteristics of eddies in the western boundary current are discussed. The energy and vorticity balance is studied in Sections 4 and 5 respectively. Finally, Section 6 is devoted to the analysis of the formation of the recirculation gyre.

For the explanation of all notations used in the paper see Part I of the study (KSPB). The description of the finite-difference scheme and numerical experiments to validate the model are given in the Appendix of KSPB.

2. The analysis of the time-averaged fields

The most remarkable feature of the problem is the formation of a recirculation gyre in the northwest corner of the basin. Figure 1 shows the time-averaged streamline patterns for several Reynolds numbers $R = 0.1, 0.4, 0.5, 0.8, 1, 1.5, 2, 3$. For small R the pattern of circulation is very close to that given by the Munk solution (Munk, 1950). However, the effect of nonlinear terms breaks the symmetry relative to $y = 0.5$, so that the maximum of the stream function is displaced to the north ($R = 0.1$). When the Reynolds number approaches 0.4, the role of advection of the

relative vorticity is increased. This leads to the formation of the separate gyre in the northwest corner of the basin. The size of the gyre is of the order of $O(\epsilon)$, the width of the boundary current.

We know from the experiments with larger ϵ (than specified in this study) that for the same R the solutions are more stable, and the recirculation gyre has a tendency of increasing its size with increasing Reynolds number while ϵ is fixed (Kamenkovich *et al.*, 1985). However, when R exceeds R_C, the solution becomes unstable and the eddies appear in the boundary current. These eddies generate Reynolds stresses that change somewhat the balance of terms in the momentum equations. As a result some broadening of the northern part of the averaged boundary current appears (Fig. 1, $R = 0.5, 0.8$) at $y = 0.7 - 0.8$. The eddies also enhance the flux of positive vorticity from the western wall to the interior part of the boundary current; therefore less amount of negative vorticity is transported to the north. As a result the size of the recirculation gyre is greatly reduced. In fact, for the Reynolds number $R = 0.8$ the local maximum of the stream function, corresponding to the recirculation gyre, is even less than that for $R = 0.4$. At the same time the local maximum of $\overline{\psi}$ in the western boundary current near $y = 0.7 - 0.8$ caused by the Reynolds stresses is very prominent for $R = 0.8$.

A different regime appears when R exceeds the second critical value $R_L = 1.6$. At such R the steady solution of the boundary layer type ceases to exist at all. The time-dependent solution can no longer be treated as a departure (even not small) from the steady solution. Alternatively, the time-averaged solution should be considered as a reference. It appears also that the eddies in the western boundary layer have limited efficiency in enhancing the flux of vorticity from the western wall. As the Reynolds number approaches R_L this eddy flux of vorticity saturates. Therefore, for $R > R_L$ nothing can stop the growth of the recirculation gyre for increasing Reynolds number, and the recirculation gyre becomes especially noticeable; the size of the gyre and characteristic velocities of circulating particles substantially increase (Fig. 1, $R = 2, 3$).

The appearance of the recirculation gyre leads to the intensification of the countercurrent located within the boundary layer to the east of the main north-going boundary current. This is clearly seen in the profiles of the meridional velocity $\overline{v}$ (Fig. 2, $R = 1, 3$). In the southern part of the basin ($y < 0.5$) the profile of $\overline{v}$ is well described by the theory of an inertial-viscous boundary layer (Kamenkovich, 1966). For $R = 3$ the splitting of the current into inertial part, with exponential velocity profile $\overline{v}(x) \sim \exp(-x/\epsilon)$, and a viscous sublayer of width $\epsilon/\sqrt{R}$ is easily seen. The countercurrent exists in the northern part of the basin ($y > 0.5$) only; it is weak near $y = 0.5$, but its intensity increases near $y = 0.7 - 0.8$. Correspondingly the maximum value of the meridional velocity in the main part of the boundary current does not decrease immediately after y exceeds 0.5. Remember that in the open ocean the

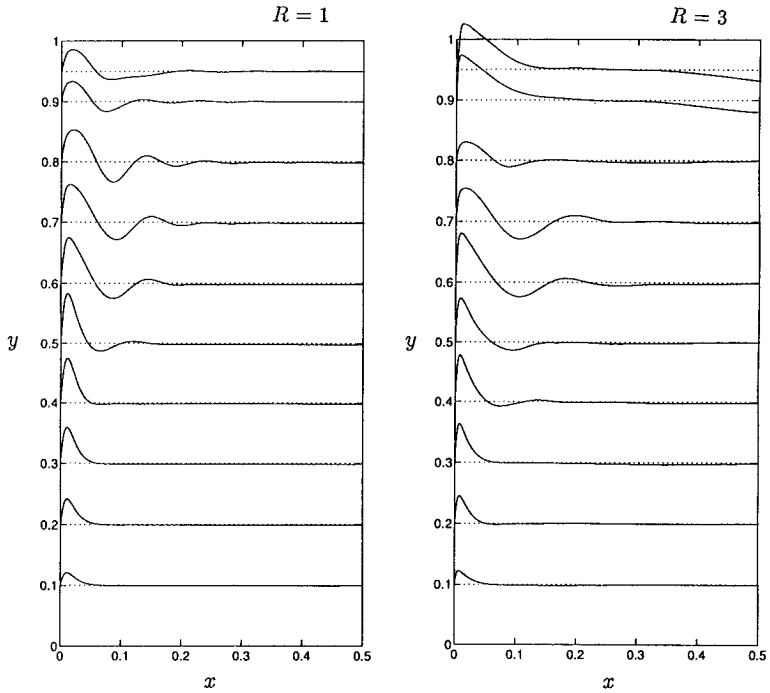

Figure 2. The profiles of the meridional velocity $\bar{v}(x)$ in the western boundary layer at $y = 0.1$; 0.2; 0.3; 0.4; 0.5; 0.6; 0.7; 0.8; 0.9; 0.95 for $R = 1$ and $R = 3$. The scale for $\bar{v}$ for all graphs remains the same; 0.1 units of y corresponds to 50 units of $\bar{v}$.

velocity is $O(1)$ whereas in the boundary layer the meridional velocity is $O(1/\epsilon)$. Therefore along every line $y = const$ the meridional velocity decays when one moves off the coast.

We now introduce the total transport of the boundary current

$$Q(y) = \int_0^{x_0} \bar{v}(x, y)\, dx \tag{1}$$

where the integral is taken from the western coast ($x = 0$) to x_0, the first zero of $\bar{v}(x)$, $x_0 \neq 0$. Figure 3 shows the graphs $Q = Q(y)$ for several R. For such a definition of Q the Munk solution ($R \ll 1$) gives $Q_{Munk}(y) = (1 + \exp(-\pi/\sqrt{3})) \sin \pi y = 1.16 \sin \pi y$, which slightly exceeds the Sverdrup transport $Q_{Sv}(y) = \sin \pi y$. However, for $R = 0.1$, when the nonlinear terms are small, the total transport for $y < 0.5$ is still close to the Sverdrup transport, $Q_{Sv}(y)$. When R increases a new maximum of Q appears near $y = 1$, Q_{RG}, due to the formation of the recirculation gyre. With the appearance of eddies in the western boundary current for $R > R_C$ the Reynolds stresses result in some increase of the averaged stream function and accordingly $Q(y)$ near $y = 0.7 - 0.8$ (Fig. 3, $R = 1$). In the interval of Reynolds numbers $R_C < R < R_L$ the maximum due to Reynolds stresses dominates the maximum Q_{RG} due

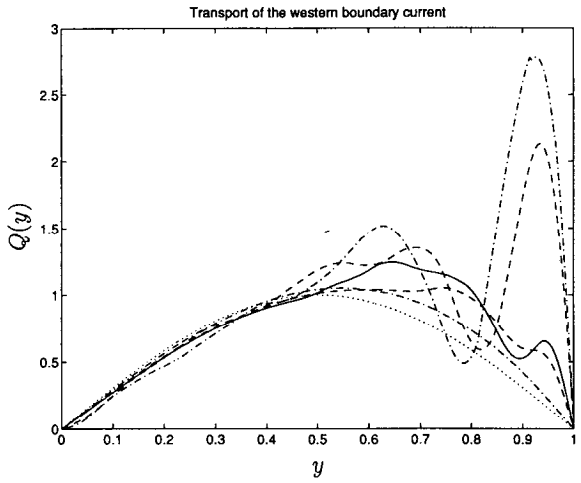

Figure 3. The total transport of the western boundary current Q as a function of latitude y for several values of $R = 0.1; 0.5; 1; 2; 3$. The solid line corresponds to $R = 1$; the dashed lines correspond to $R = 0.5; 2$; the dot-dashed lines correspond to $R = 0.1; 3$. The curves for $R = 2; 3$ have prominent maxima near $y = 1$ due to the formation of recirculation gyre. The dotted line shows the Sverdrup transport, $Q_{Sv} = \sin \pi y$.

to the recirculation gyre, but as the Reynolds number exceeds R_L the recirculation gyre becomes very prominent (Fig. 3, $R = 2, 3$). For $R = 3$ the maximum Q_{RG} is substantially larger than the maximum Sverdrup transport at $y = 0.5$. Note that, according to observations, the ratio of these maxima $Q_{RG}/Q_{Sv}(0.5)$ is approximately equal to 3 (Ierley, 1990). We stress that $Q(y)$ is close to $Q_{Sv}(y)$ for all R when $y < 0.5$.

One's first impression is that the total transport of the recirculation gyre Q_{RG} should increase monotonically with increasing R. However, as we have already mentioned, the eddies in the western boundary current produce the Reynolds stresses that significantly influence the size of the recirculation gyre. Thus, a complicated behavior of $Q_{RG}(R)$ (Fig. 4) occurs. When R exceeds $R_C = 0.38$, Q_{RG} even slightly decreases. In the interval $R_C < R < R_L$ the eddies in the western boundary layer efficiently fight the growth of the recirculation gyre. We see that a noticeable growth of Q_{RG} starts only when $R > R_L$. This means that the rapid growth of the recirculation gyre with increasing Reynolds number and the breakdown of the boundary layer type solution at $R = R_L$ are two closely related phenomena.

Figure 5 shows the distribution of the averaged relative vorticity $\bar{\omega}$ for $R = 1$ and 2. We see that strong gradients of $\bar{\omega}$ exist near the western coast only. There are moderate gradients (compared to those near the western boundary) of $\bar{\omega}$ near the northern boundary, even in the region of the recirculation, despite the presence of the strong currents there. It is interesting to note the existence of the extremum of $\bar{\omega}$ in the recirculation gyre, though it is displaced north relative to the gyre center.

Let us consider the isolines of the averaged potential vorticity $\bar{q}$, $\bar{q} = y + \epsilon^2\bar{\omega}$, and

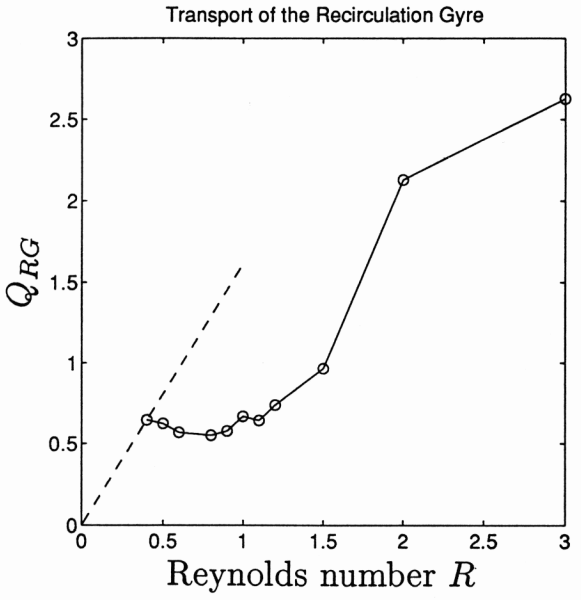

Figure 4. The transport of the recirculation gyre Q_{RG}. The dashed line shows the estimate if the solution were stable and eddies did not form in the western boundary layer.

isolines of the averaged stream function $\overline{\psi}$ simultaneously. In this way the regions, where the effects of vorticity diffusion and external forcing are of substantial influence, are easily identified. Figure 6 shows the isolines of $\overline{q}$ and $\overline{\psi}$ in the boundary layer and in the recirculation zone for $R = 1$ and 2. In the open ocean the relative vorticity $\epsilon^2\overline{\omega}$ is small which is why the isolines of $\overline{q}$ are very close to lines $y = const.$ In the inertial part of the boundary layer the isolines of $\overline{q}$ and $\overline{\psi}$ nearly coincide because of the conservation of the potential vorticity $\overline{q}$. Within the viscous sublayer near the coast the diffusion of $\overline{\omega}$ is substantial. It causes the intersection of isolines of $\overline{q}$ and $\overline{\psi}$: a fluid particle moving along a $\overline{\psi}$-isoline increases its potential vorticity. It is worth noting that the density of $\overline{q}$-isolines near the coast differs for different y, which indicates a latitude-dependent rate of diffusion of $\overline{\omega}$ from the coast (Fig. 6). The maximum density of $\overline{q}$-isolines is observed at $y \sim 0.5$. However, in the northern part of the boundary layer, there are several extrema of the $\overline{q}$-isoline density (minimum at $y \sim 0.81$, maximum at $y \sim 0.91$, (Fig. 6, $R = 2$)). This is due to the influence of the recirculation gyre on the structure of the currents in this area. Near $y \sim 0.91$ the recirculation gyre forces the boundary current to press more strongly against the western coast thus sharpening the gradient of $\overline{q}$ in this region (see also Section 5).

Figure 6 shows very clearly those regions in the recirculation gyre when the vorticity diffusion and/or external forcing are important. It is apparent by eye that, in the central part of the recirculation gyre and in the vicinity of the northern boundary, the isolines of $\overline{q}$ and $\overline{\psi}$ coincide. The motion there is therefore inertial, i.e., each fluid

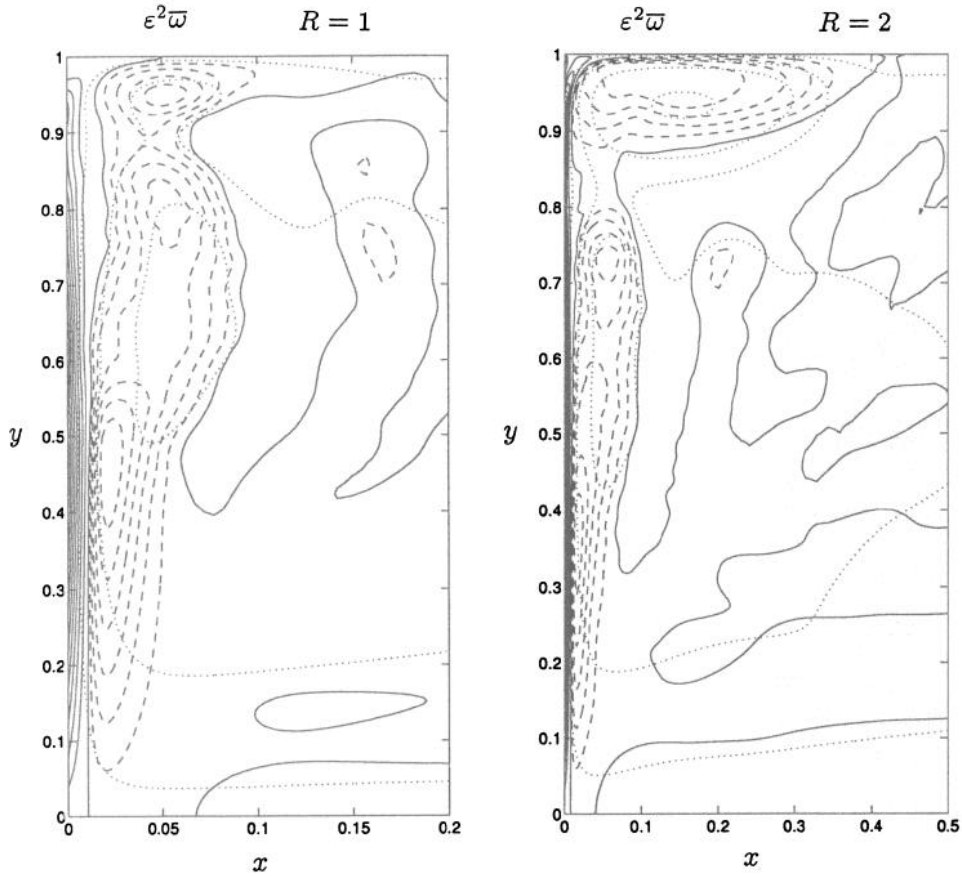

Figure 5. The relative vorticity $\epsilon^2\overline{\omega}$ of the time-averaged solution for $R = 1$ and $R = 2$ within the western boundary layer. The negative isolines (dashed) are drawn with the contour interval, $CI = 0.025$; the positive isolines (solid)—with $CI = 0.1$. The dotted isolines show the typical time-averaged streamlines $\overline{\psi} = 0.1; 0.5; 1; 2$.

particle conserves its potential vorticity.[4] The diffusion and forcing are substantial in the western near-coast part of the gyre and near its southeast edge. In the latter region the fluid particles move along messy loop-like trajectories. It is worth remembering that the isolines of the time-averaged stream function $\overline{\psi}$ do not coincide with the trajectories of the particles in the time-dependent motion.

It is useful also to consider scatterplots of $\overline{q}$ vs. $\overline{\psi}$ (Fig. 7). Each point of our nonuniform grid generates one point $(\overline{\psi}, \overline{q})$ in the scatterplot. The region $0 < \overline{\psi} < \sin \pi\overline{q}$ in the scatterplot corresponds to the Sverdrup (interior) solution; the points near $\overline{\psi} = 0$ that have increased values of $\overline{q}$ correspond to the western boundary

4. The inertial character of the motion within the recirculation gyre was noted also by Böning (1986) in a series of numerical runs with slip boundary conditions at the coasts.

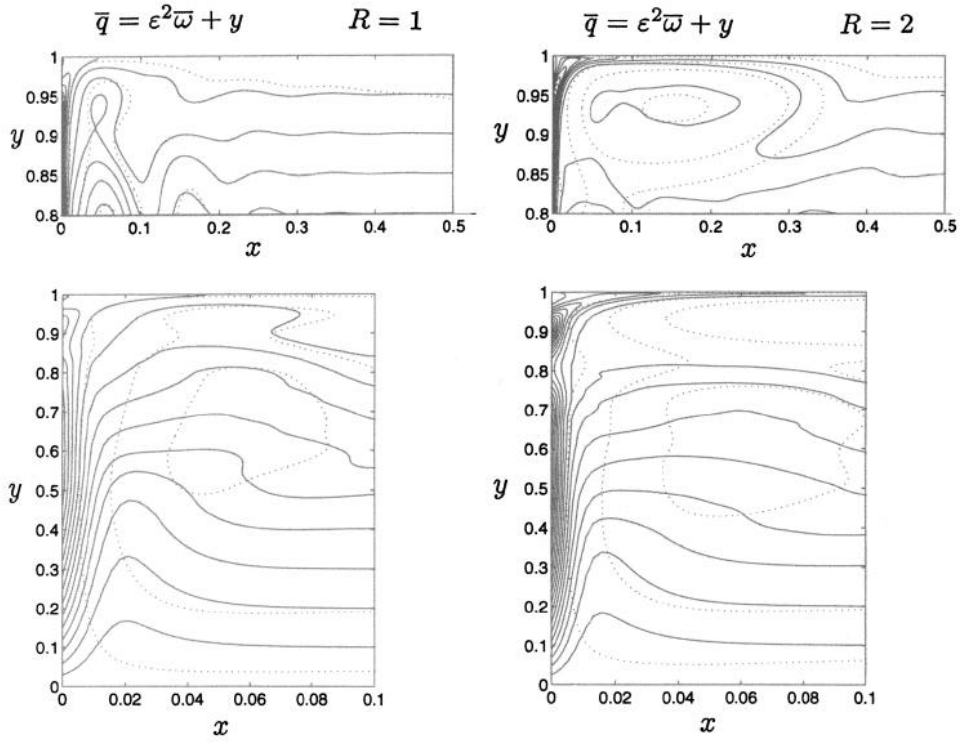

Figure 6. The potential vorticity $\overline{q} = \epsilon^2\overline{\omega} + y$ of the time-averaged solution within the western boundary layer ($CI = 0.1$) and in the recirculation gyre zone ($CI = 0.05$) for two values of R. The typical time-averaged streamlines $\overline{\psi} = 0.1; 0.5; 1; 2$ are shown by dotted lines.

current. The points $(\overline{\psi}, \overline{q})$, corresponding to the recirculation gyre, have a tendency to be located along a straight line. For $R = 1.5$ this tendency is not yet very clearly revealed, but for $R = 2$ (Fig. 7) it is quite distinct already. Thus, for $R = 2$ we find approximately

$$\overline{q} = a + b\overline{\psi}, \qquad a = 0.92, \qquad b = -0.033. \tag{2}$$

The functional relation of $\overline{q}$ with $\overline{\psi}$ gives one more evidence that the movement of particles in the main part of the recirculation gyre is predominantly inertial. However, the small effects of vorticity diffusion and the external source of vorticity are crucial to determine the sign and magnitude of b or, more generally, $d\overline{q}/d\overline{\psi}$ (see also Marshall and Marshall, 1992). Indeed, integrating the time-averaged vorticity equation (see (12) of KSPB or (28) from Section 5) over the region enclosed by the isoline $\overline{\psi} = const$ and neglecting for simplicity the contribution of the eddy motion into the vorticity diffusion gives

$$\int\int_{\overline{\psi}} (\gamma^3 \Delta\overline{q} + \nabla \times \tau)\, dx\, dy = 0. \tag{3}$$

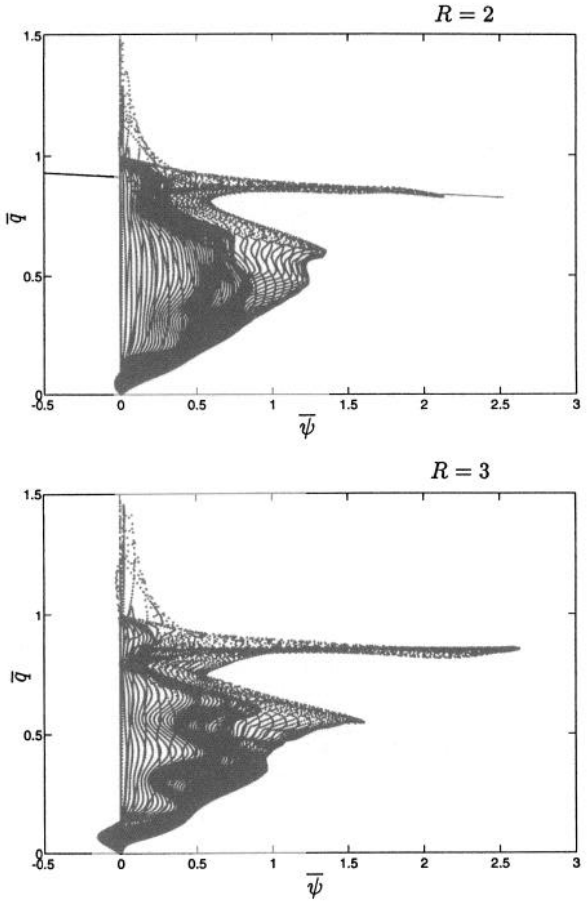

Figure 7. The scatterplot of $\overline{q}$ vs. $\overline{\psi}$ for the time-averaged solution for $R = 2$ and $R = 3$. To produce the scatterplot $\overline{q}$ and $\overline{\psi}$ are evaluated simultaneously in all grid points.

If we assume that the $\overline{\psi}$-isoline is so chosen that it encloses the inertial part of the recirculation zone we can insert relation (2) in (3) to obtain

$$\int\int_{\overline{\psi}} (\gamma^3 b \Delta \overline{\psi} + \nabla \times \tau)\, dx\, dy = 0. \tag{4}$$

For the recirculation gyre the relative vorticity $\overline{\omega} = \Delta\overline{\psi}$ is negative (Fig. 5). Thus, to balance the negative $\nabla \times \tau$ we must have $b < 0$. If we use numerical values of $\Delta\overline{\psi}$ and $\nabla \times \tau$ for the center of the recirculation gyre it results from (4) that b is close to the value given in (2).

It should be noted that for $R = 2$ we do not have, strictly speaking, the homogenization of the potential vorticity $\overline{q}$ in the recirculation gyre: b is small but it is not equal to zero. Besides, there is a noticeable blurring of the $(\overline{\psi}, \overline{q})$ relation in the recirculation gyre indicating redistribution of potential vorticity from one part of the

gyre to another. All this means that for $R = 2$ both viscosity and external forcing are important in the dynamics of the recirculation gyre. For $R = 3$ however the situation changes. The role of eddies in comparison to explicit viscosity increases (see Section 5) and the homogenization of potential vorticity becomes more prominent, and the line representing the $(\bar{\psi}, \bar{q})$ relation becomes more horizontal (Fig. 7).

3. Eddies in the boundary current

The formation of eddies in the western boundary current is a characteristic property of our solution (Fig. 1, KSPB). Similar eddies have also been observed in the numerical experiments of Bryan (1963). They are formed near the point $y = 0.5$ where the Sverdrup transport reaches its maximum. Then they move northward with the current and eventually are absorbed by the recirculation gyre. In this section we will examine some of the quantitative characteristics of these eddies more closely.

First, it is useful to look at the eddies on an enlarged scale. Figure 8 shows the instantaneous field ψ at time $t = 10000$. (Recall that the averaging of ψ in the experiment *R1M* (KSPB, Table 1) was performed over the time interval (5000, 10000).) Figure 8b shows the time-averaged field $\bar{\psi}$ whereas Figure 8c gives the deviation from $\bar{\psi}$: $\psi' = \psi - \bar{\psi}$. Although we can see in Figure 8a anticyclonic eddies only, Figure 8c shows clearly both positive and negative deviations from the averaged field, with negative deviations corresponding to the troughs between the eddies. The eddies considered are evidently highly nonlinear since their amplitudes are comparable with the characteristic velocities of the mean current.

To check that these eddies are not due to some kind of numerical instability we present the potential vorticity, $q = \epsilon^2\omega + y$, in Figure 8d. One can see that q inside the eddies remains within the physical limits. Note that the potential vorticity is increased near the boundary at approximately the same latitude y as the position of the eddy center. We can also see that the tongue of increased potential vorticity is swept to the inertial part of the boundary layer by the circulation within the eddy. By this mechanism the eddies enhance the transfer of positive vorticity from the boundary.

The velocity of eddy translation $c = dy/dt$ can be determined, for example, visually by following the translation of the eddy center. However, when the Reynolds number R approaches R_L eddy movement becomes noticeably chaotic and it becomes somewhat difficult to trace each individual eddy. Alternatively, one can determine c by computing the time-lagged correlations between the time records of the stream function at different points in the boundary layer. (The time records of the stream function were discussed in KSPB, Section 4.) For our purpose it is convenient to consider the time-lagged correlation $C_{78}(\tau) = \overline{\psi(x_C, 0.7, t) \cdot \psi(x_C, 0.8, t + \tau)}$ between points with $y = 0.7$ and $y = 0.8$ ($x_C = 5.1530 \cdot 10^{-2}$). In this formula the overbar means time averaging and τ is the time lag. (In computing the correlation it is necessary to remove the mean from the time records.) If it takes an eddy the time

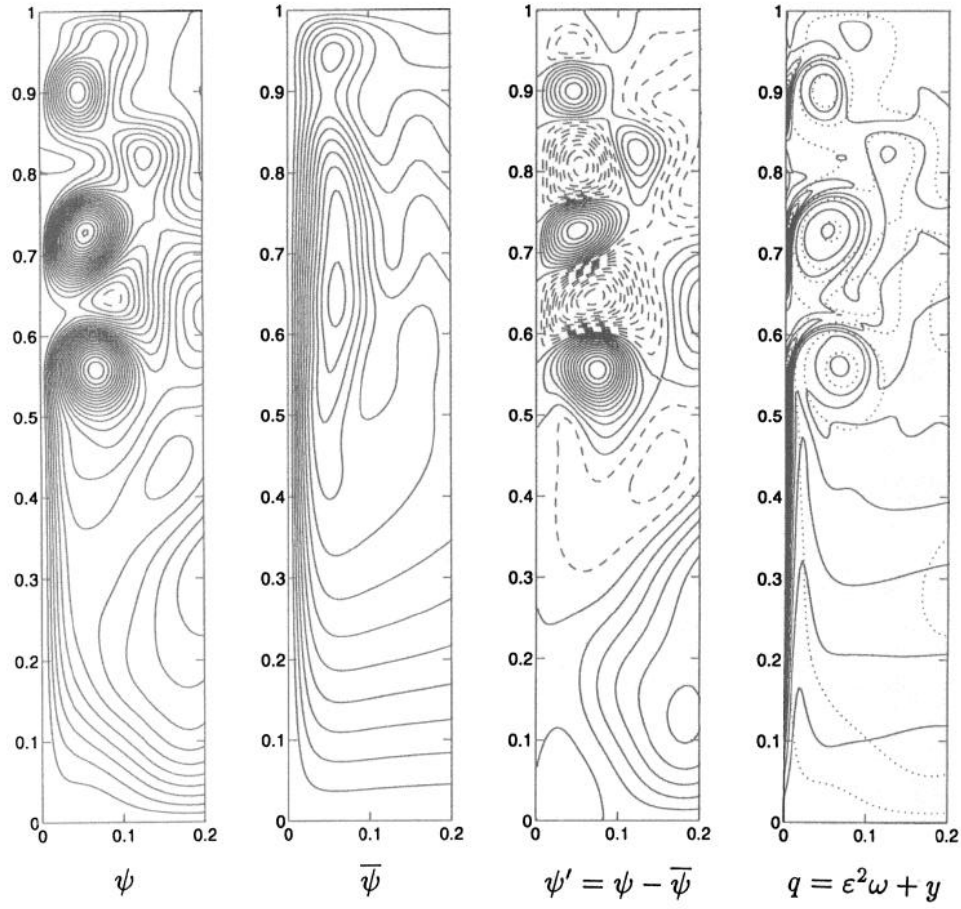

Figure 8. The eddies in the western boundary current in the experiment *R1M* shown on the expanded scale. (a) The instantaneous field ψ at time $t = 10000$, the contour interval, $CI = 0.1$; (b) The time-averaged field $\overline{\psi}^M$, $CI = 0.1$; (c) Departures from the mean field $\psi' = \psi(t = 10000) - \overline{\psi}^M$, $CI = 0.1$; (d) The potential vorticity field $\overline{q} = \epsilon^2\overline{\omega} + y$ at time $t = 10000$, $CI = 0.1$. The typical time-averaged streamlines $\overline{\psi}^M = 0.1$; 0.5; 1; 2 are shown by dotted lines.

$\tau_1 = \Delta y/c$ to cover the distance $\Delta y = 0.1$ between the two points, then the correlation function $C_{78}(\tau)$ will have a maximum at $\tau = \tau_1$. In Figure 9a we present the correlation $C_{78}(\tau)$ obtained in the experiment *R1M* by averaging over the time interval (5000, 10000). The first maximum ($\tau > 0$) appears at $\tau = \tau_1 = 152$, which gives the eddy translation speed $c = 6.58 \cdot 10^{-4}$.

Periodicity of the eddy formation T_e ($\sigma_e = 2\pi/T_e$) can be determined by taking the Fourier transform of the time records of the stream function in the boundary layer (as in KSPB) or, alternatively, by computing the autocorrelation function. Figure 9b

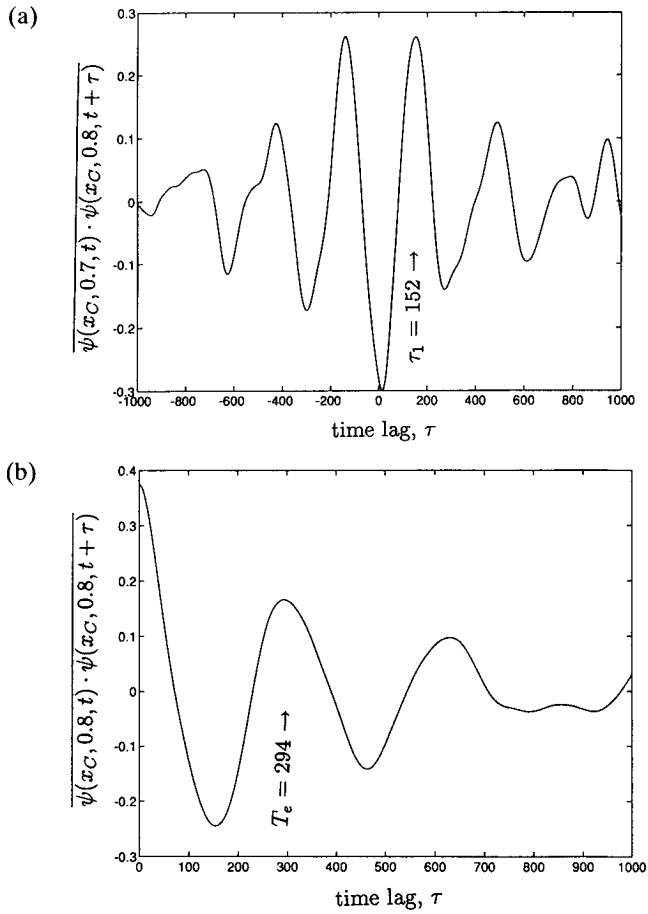

Figure 9. The correlation functions of the time records of the stream function in the boundary layer in the experiment *R1M*. (a) The time-lagged correlation $C_{78}(\tau) = \overline{\psi(x_C, 0.7, t) \cdot \psi(x_C, 0.8, t+\tau)}$between points with $y = 0.7$ and $y = 0.8$ ($x_C = 5.1530 \cdot 10^{-2}$). (b) The autocorrelation function $C_{88}(\tau) = \overline{\psi(x_C, 0.8, t) \cdot \psi(x_C, 0.8, t+\tau)}$for the point $x_C, y = 0.8$.

shows the autocorrelation function $C_{88}(\tau) = \overline{\psi(x_C, 0.8, t) \cdot \psi(x_C, 0.8, t+\tau)}$ for the point x_C, $y = 0.8$ in the experiment *R1M*. Since the eddies cause the dominant perturbations of the stream function in the boundary layer the function $C_{88}(\tau)$ has a prominent maximum at $\tau = T_e = 294$ corresponding to the periodicity of eddy formation. Knowing c and T_e allows us to determine the averaged spacing between eddies $\lambda_e = cT_e$.

Applying the same method to the time records of the stream function from other experiments *R0.8M*, *R0.5M* and summarizing the results gives the following characteristics of eddies: $R = 0.5, c = 7.57 \cdot 10^{-4}, T_e = 233, \sigma_e = 2.70 \cdot 10^{-2}, \lambda_e = 0.177; R = 0.8,$

$c = 6.94 \cdot 10^{-4}$, $T_e = 268$, $\sigma_e = 2.34 \cdot 10^{-2}$, $\lambda_e = 0.186$; $R = 1$, $c = 6.58 \cdot 10^{-4}$, $T_e = 294$, $\sigma_e = 2.14 \cdot 10^{-2}$, $\lambda_e = 0.193$. For R exceeding R_L the motions in the boundary layer become substantially more chaotic and the determination of the above quantities becomes ambiguous.

It is worth noting that the eddy centers move near the line of vanishing $\overline{\omega}_x$, i.e. near the inflection point of the velocity profile of the current. This is a critical point according to the theory of stability (Drazin and Reid, 1981). At this point the velocity of the time-averaged current itself is close to the speed of eddy translation c.

It is reasonable to assume that the appearance of the eddies in the boundary layer is a result of an instability of the boundary current. The analysis by Ierley and Young (1991) of the stability of the Munk boundary current by idealizing it as a parallel flow shows that the slip case should be more unstable than the no-slip case. However, as mentioned earlier, the eddies in the boundary layer do not appear when the slip boundary conditions are specified at the coasts (Fig. 3, KSPB). This result is supported by altnernative experiments (see Böning, 1986) as well. One may speculate that the onset of the recirculation gyre strongly alters the basic state of the stability problem and thus corresponding stability conditions of Ierley and Young (1991). Another point is that one should make a distinction between *convected instability* and *absolute* or *non-convected instability* (see, for example, Drazin and Reid (1981)). In Cessi and Ierley (1993) it is suggested that with the Munk profile in the no-slip case the group velocity of disturbance c_g is close to zero, and the disturbance can grow very efficiently (absolute instability), while in the slip case the group velocity is sufficiently large, and the perturbation (though convectively unstable) will move away from the unstable region. Detailed exploration of the 2D stability problem is considered in SIK.

4. The energy balance

The energy equation is derived in the usual way by multiplying the momentum equations (1)–(2) from KSPB scalarly by the velocity $\mathbf{v} = (u, v)$ to obtain

$$\begin{aligned}\frac{\partial E}{\partial t} + \frac{\partial}{\partial x}\left[\left(\epsilon^2 E + p - 2\gamma^3 \frac{\partial u}{\partial x}\right)u - \gamma^3\left(\frac{\partial v}{\partial x} + \frac{\partial u}{\partial y}\right)v\right] \\ + \frac{\partial}{\partial y}\left[\left(\epsilon^2 E + p - 2\gamma^3 \frac{\partial v}{\partial y}\right)v - \gamma^3\left(\frac{\partial v}{\partial x} + \frac{\partial u}{\partial y}\right)u\right] \\ = -\gamma^3\left[2\left(\frac{\partial u}{\partial x}\right)^2 + \left(\frac{\partial v}{\partial x} + \frac{\partial u}{\partial y}\right)^2 + 2\left(\frac{\partial v}{\partial y}\right)^2\right] + u\tau^{(x)} = -D + W\end{aligned} \tag{5}$$

where $E(x, y, t) = \frac{1}{2}(\nabla\psi)^2 = \frac{1}{2}(u^2 + v^2)$ is the density of kinetic energy. On the right-hand side of (5) we have viscous dissipation $D(x, y, t)$ and work of the wind stress $W(x, y, t)$ per unit time. The Coriolis force does not perform any work.

Integrating (5) over the basin and taking into account the boundary conditions

((4), (5) from KSPB) gives

$$\frac{d\langle E\rangle(t)}{dt} = -\langle D\rangle(t) + \langle W\rangle(t) \tag{6}$$

where

$$\begin{aligned}\langle E\rangle(t) &= \int_0^1\int_0^1 E\,dx\,dy;\\ \langle D\rangle(t) &= \int_0^1\int_0^1 D\,dx\,dy;\\ \langle W\rangle(t) &= \int_0^1\int_0^1 W\,dx\,dy.\end{aligned} \tag{7}$$

It is helpful to start with the consideration of the energy balance for the steady linear Munk solution. The solution in this case can be represented as the sum of the Sverdrup solution (SV) in the interior and the boundary layer solution (BL)

$$\psi_M(x,y) = \psi_{SV}(x,y) + \psi_{BL}\left(\frac{x}{\gamma},y\right) + O(\gamma) \tag{8}$$

$$\psi_{SV}(x,y) = (1-x)\sin \pi y \tag{9}$$

$$\psi_{BL\,N} = -e^{-\xi/2}\left(\cos\frac{\sqrt{3}}{2}\xi + \frac{1}{\sqrt{3}}\sin\frac{\sqrt{3}}{2}\xi\right)\sin \pi y, \quad \text{no-slip} \quad \frac{\partial\psi_{BL\,N}}{\partial\xi}(0,y) = 0 \tag{10}$$

$$\psi_{BL\,S} = -e^{-\xi/2}\left(\cos\frac{\sqrt{3}}{2}\xi - \frac{1}{\sqrt{3}}\sin\frac{\sqrt{3}}{2}\xi\right)\sin \pi y, \quad \text{slip} \quad \frac{\partial^2\psi_{BL\,S}}{\partial\xi^2}(0,y) = 0 \tag{11}$$

where we have introduced the stretched variable $\xi = x/\gamma$, $\gamma \ll 1$. The structure of the western boundary layer current depends on the type of dynamical boundary condition (the subscripts N, S). It is very easy to show that the major contribution to the total kinetic energy $\langle E\rangle$ is due to the western boundary layer only which is why we do not consider here the boundary layers near the eastern, southern, and northern boundaries

$$\begin{aligned}\langle E\rangle[\psi_M] &= \frac{1}{\gamma}\int_0^1\int_0^\infty \frac{1}{2}\left(\frac{\partial\psi_{BL}(\xi,y)}{\partial\xi}\right)^2 d\xi\,dy + O(1)\\ &= \begin{cases}1/(8\gamma) + O(1), & \text{no-slip}\\ 1/(4\gamma) + O(1), & \text{slip}\end{cases}.\end{aligned} \tag{12}$$

We see that $\langle E\rangle[\psi_M]$, which is actually the kinetic energy of the boundary layer current, in the slip case is two times bigger than in the no-slip case. It seems that this fact can explain why in the nonlinear case for the same Reynolds number the recirculation gyre is larger in the slip case as compared to the no-slip case. Indeed,

the larger the energy of the boundary current, the higher absolute velocities of the fluid particles, the larger inertia of the boundary current in the nonlinear case, the less efficient are the viscous forces in decelerating the current, the stronger the current impinges on the northern boundary, and finally the larger the recirculation gyre which forms in the northwest corner. It is worth noting that the splitting of the inertial-viscous boundary current into an inertial part and a viscous sublayer of width $\epsilon/\sqrt{R}$ also takes place in the slip case, but the change of velocity in the viscous sublayer is not so substantial as in the no-slip case. Recall that in the slip case the vorticity is equal to zero at the western boundary.

Similarly, the major contribution to the dissipation is also due to the western boundary current

$$\langle D\rangle[\psi_M] = \int_0^1\int_0^\infty \frac{\partial^2\psi_{BL}}{\partial\xi^2}\frac{\partial^2\psi_{BL}}{\partial\xi^2}\,d\xi\,dy + O(\gamma) = \frac{1}{4} + O(\gamma). \tag{13}$$

Dissipation is the same both in the no-slip and slip cases.

On the other hand, the energy input, which is due to the work of the wind stress, is determined by the Sverdrup solution

$$\langle W\rangle[\psi_M] = -\int_0^1\int_0^1 \frac{\partial\psi_{SV}}{\partial y}\tau^{(x)}\,dx\,dy + O(\gamma) = \frac{1}{4} + O(\gamma). \tag{14}$$

We see that, for the steady Munk solution, the energy equation (6) is trivially satisfied.

When $R \ll 1$ the solution of the problem (1)–(6) from KSPB is very close to the Munk solution. Thus, we can conclude that the level of the total kinetic energy for $R \ll 1$ is determined by the width of the viscous boundary layer $\gamma = \epsilon/\sqrt[3]{R}$. Using energy considerations we can obtain the estimate for the time of the formation of the boundary layer for $R \ll 1$

$$t \sim \frac{\langle E\rangle}{\langle W\rangle} \sim \frac{1/8\gamma}{1/4} \sim O\left(\frac{1}{\gamma}\right). \tag{15}$$

It is useful to compare this with the result of the linear theory for an accelerating boundary layer (see, for example, Kamenkovich, 1977, Section 6.7): the width δ_T of the nonstationary boundary current decreases with time during the spin-up regime, $\delta_T \sim 1/t$, until δ_T becomes comparable with γ and the viscous effects arrest further thinning of the boundary layer.

The total kinetic energy is a useful global characteristic of time variability of the system. However, not all the modes manifest themselves equally. Let us give this question a closer look. It is helpful to consider the oscillations of the total kinetic energy in the following way. We start with $R \ll 1$ and represent the solution of the problem to a certain approximation as a sum of the Munk solution $\psi_M(x, y)$ and a

basin mode $\psi_{nm}(x, y, t)$ (see (16) from KSPB). We have

$$\langle E\rangle[\psi_M + \psi_{nm}] = \int_0^1 \int_0^1 \left(\frac{1}{2}\nabla\psi_M \cdot \nabla\psi_M + \frac{1}{2}\nabla\psi_{nm} \cdot \nabla\psi_{nm} + \nabla\psi_M \cdot \nabla\psi_{nm}\right) dx\, dy. \quad (16)$$

Consider each term on the right-hand side of (16) separately. The first term gives the kinetic energy of the steady Munk solution and does not depend on t. For the inviscid problem the second term, representing the kinetic energy of the basin mode, would not also depend on t. But in the presence of small dissipation this term slowly decreases. The third term, the cross term, causes the oscillation of the total kinetic energy with the eigenfrequency, σ_{nm}, of the basin mode if the corresponding expression is not identically zero. In the problem considered we use a very special wind stress distribution with only one Fourier harmonic, $\sin \pi y$, therefore the Munk solution also has the form $\psi_M \sim \sin \pi y$. Thus all basin modes with $m \neq 1$ are orthogonal to the Munk solution and hence the cross term for these modes equals zero.

It follows from the energy balance equation (6) that the energy oscillations are connected with variation of the rate of dissipation and variation of the rate of energy input. Scale analysis shows that the variation of the rate of energy input is the leading factor. With the same approximation, we have

$$\langle W\rangle[\psi_M + \psi_{nm}] = \int_0^1 \int_0^1 \left(-\frac{\partial\psi_M}{\partial y}\tau^{(x)} - \frac{\partial\psi_{nm}}{\partial y}\tau^{(x)}\right) dx\, dy. \quad (17)$$

We see that it is the second term on the right-hand side of (17) that causes the oscillation of energy with the frequency of the basin mode σ_{nm}.

In considering the total energy oscillations due to basin modes we have made the assumption that $R \ll 1$. However, the same arguments hold also for finite R if the time-averaged solution does not differ substantially from the linear one. For example, we present in Figure 10 the time variations of $\langle E\rangle, d\langle E\rangle/dt, \langle D\rangle, \langle W\rangle$ for $R = 1$. It is seen that in the experiment *R1Z* (with zero initial conditions) (Fig. 10a) the amplitude of the basin mode ψ_{11} becomes prominent after the spin-up, which is why the oscillations of $d\langle E\rangle/dt$ and $\langle W\rangle$ are in phase and have the dominant frequency σ_{11}. The oscillations of $\langle D\rangle$ and $\langle W\rangle$ take place around the levels approximately determined by (13) and (14). Note that the amplitude of variation of dissipation is small. Figure 10b gives the time variations of the same quantities but in the experiment *R1M* (started from the time-averaged field). The basin mode ψ_{11} has been already filtered out, and after reaching the quasistationary regime the oscillations take place at different frequencies characterizing the periodicity of the eddy formation in the boundary layer. For $R > 1$, when the time-averaged circulation differs noticeably from the Munk solution, the cross term in (17) is not identically zero for $m \neq 1$, hence all basin modes can manifest themselves in the variation of the total kinetic energy.

Let us consider now the general nonlinear case when the problem (1)–(6) from

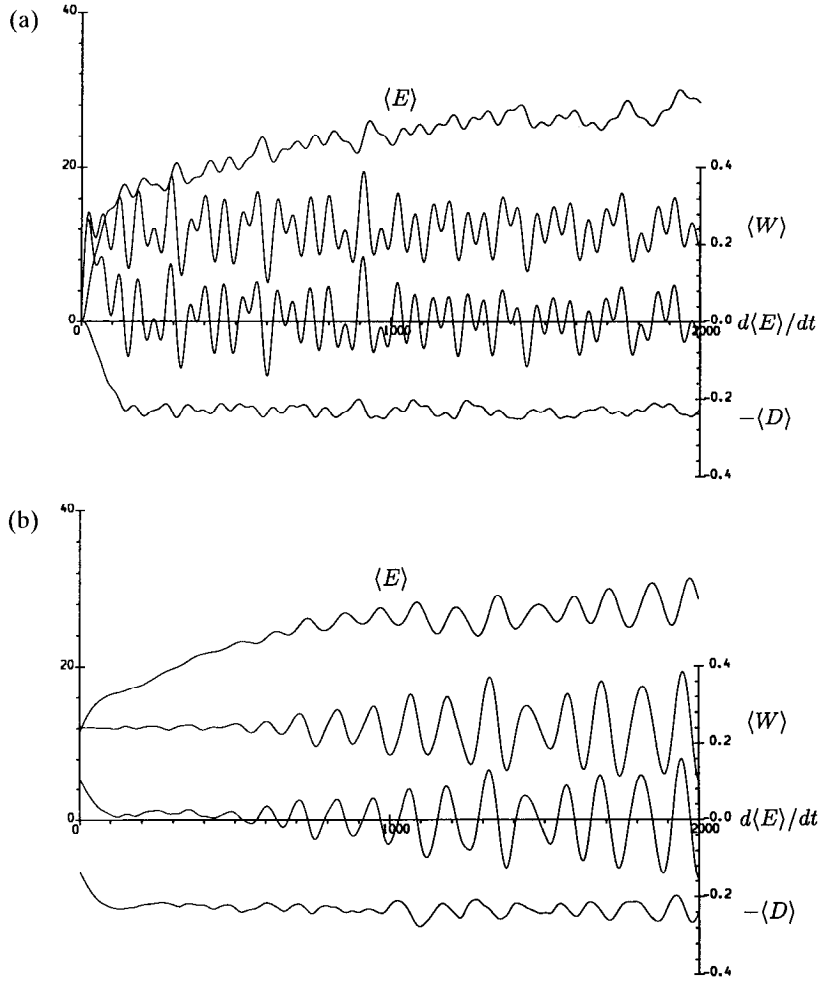

Figure 10. The time variation of the terms in the energy equation (6) in the experiments with $R = 1$: (a) $R1Z$; (b) $R1M$. The uppermost curve is the total energy, $\langle E\rangle(t)$, the scale is given at the left. The other three curves (scale is given at the right) are the work of the wind $\langle W\rangle(t)$ (oscillating around 0.25), the time derivative of the total energy $d\langle E\rangle(t)/dt$ (oscillating around 0), and the viscous dissipation of energy $-\langle D\rangle(t)$ (oscillating around -0.25).

KSPB cannot have a steady solution. It is natural to analyze the energy balance for the time-averaged current and also the energetics of "eddies" or "pulsations" determined as departures from the time-averaged fields. Keeping this in mind, we introduce the kinetic energy of the time-averaged current $E_m = \frac{1}{2}(\overline{u}^2 + \overline{v}^2)$, the averaged energy $\overline{E} = \frac{1}{2}\overline{(u^2 + v^2)}$, and the "eddy" kinetic energy $E_e = \frac{1}{2}\overline{((u')^2 + (v')^2)}$.

In the usual way we obtain the following equations

$$\frac{\partial}{\partial x}\left[\left(\epsilon^2 E_m + \bar{p} - 2\gamma^3 \frac{\partial \bar{u}}{\partial x} + \epsilon^2 \overline{u'^2}\right)\bar{u} + \left(-\gamma^3\left(\frac{\partial \bar{v}}{\partial x} + \frac{\partial \bar{u}}{\partial y}\right) + \epsilon^2 \overline{u'v'}\right)\bar{v}\right]$$
$$+ \frac{\partial}{\partial y}\left[\left(\epsilon^2 E_m + \bar{p} - 2\gamma^3 \frac{\partial \bar{v}}{\partial y} + \epsilon^2 \overline{v'^2}\right)\bar{v} + \left(-\gamma^3\left(\frac{\partial \bar{v}}{\partial x} + \frac{\partial \bar{u}}{\partial y}\right) + \epsilon^2 \overline{u'v'}\right)\bar{u}\right] + G \tag{18}$$
$$= -D_m + W_m$$

$$\frac{\partial}{\partial x}\left[\epsilon^2 E_e \bar{u} - \gamma^3\left(2\overline{\frac{\partial u'}{\partial x}u'} + \overline{\left(\frac{\partial v'}{\partial x} + \frac{\partial u'}{\partial y}\right)v'}\right) + \overline{p'u'} + \frac{\epsilon^2}{2}(\overline{u'^3} + \overline{u'v'^2})\right]$$
$$+ \frac{\partial}{\partial y}\left[\epsilon^2 E_e \bar{v} - \gamma^3\left(2\overline{\frac{\partial v'}{\partial y}v'} + \overline{\left(\frac{\partial v'}{\partial x} + \frac{\partial u'}{\partial y}\right)u'}\right)\right. \tag{19}$$
$$\left. + \overline{p'v'} + \frac{\epsilon^2}{2}(\overline{v'^3} + \overline{u'^2 v'})\right] - G = -D_e$$

where

$$G = -\epsilon^2\left[\overline{u'^2}\frac{\partial \bar{u}}{\partial x} + \overline{u'v'}\left(\frac{\partial \bar{v}}{\partial x} + \frac{\partial \bar{u}}{\partial y}\right) + \overline{v'^2}\frac{\partial \bar{v}}{\partial y}\right]$$
$$D_m = \gamma^3\left[2\left(\frac{\partial \bar{u}}{\partial x}\right)^2 + \left(\frac{\partial \bar{v}}{\partial x} + \frac{\partial \bar{u}}{\partial y}\right)^2 + 2\left(\frac{\partial \bar{v}}{\partial y}\right)^2\right] \tag{20}$$
$$D_e = \gamma^3\left[2\overline{\left(\frac{\partial u'}{\partial x}\right)^2} + \overline{\left(\frac{\partial v'}{\partial x} + \frac{\partial u'}{\partial y}\right)^2} + 2\overline{\left(\frac{\partial v'}{\partial y}\right)^2}\right]$$
$$W_m = \bar{u}\tau^{(x)}.$$

In these relations it is implied that $\partial E_m/\partial t = 0$, $\partial E_e/\partial t = 0$, and $\overline{E} = E_m + E_e$. We have introduced also the following notations: G is the density of the energy flux from the averaged motion to the eddy or pulsation motion, D_m is the density of dissipation in the averaged motion per time unit, D_e is the density of dissipation in the eddy motion per time unit, and W_m is the work performed by the wind stress in the averaged motion (per square and time units).

Integrating relations (18) and (19) over the basin gives the following balances:

$$\langle W_m \rangle = \langle D_m \rangle + \langle G \rangle \tag{21}$$

$$\langle G \rangle = \langle D_e \rangle \tag{22}$$

where the values integrated over the basin are introduced similarly to (7). Relation (21) means that the total energy input into the system by the wind, $\langle W_m \rangle$, is balanced

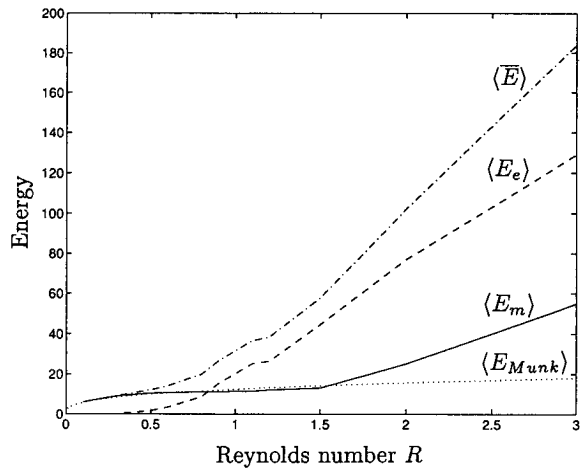

Figure 11. The partitioning of total energy $\langle \overline{E} \rangle$ (dash-dotted line) in the quasi-stationary regime between the energy of the mean flow $\langle E_m \rangle$ (solid line) and the energy of eddies $\langle E_e \rangle$ (dashed line) for various Reynolds number R in the experiments with $\epsilon = 0.01$, no-slip. The dotted line shows the energy of the Munk solution $\langle E_{Munk} \rangle = 1/(8\gamma)$ for the corresponding viscosity $\gamma = \epsilon/\sqrt[3]{R}$.

by the total dissipation in the mean motion, $\langle D_m \rangle$, and total transfer of energy from the averaged motion to the eddy motion (per time unit), $\langle G \rangle$. Eq. (22) states that the total energy transfer from the averaged motion to the eddy motion is balanced by total dissipation in the eddy motion, $\langle D_e \rangle$.

Let us discuss now what is observed in the numerical experiments. Figure 11 shows the partitioning of the averaged kinetic energy of the system between the mean current and eddy motion as a function of Reynolds number. The kinetic energy of the linear Munk solution $\langle E_{Munk} \rangle = 1/(8\gamma)$ for the corresponding viscosity $\gamma = \epsilon/\sqrt[3]{R}$ (see (12)) is shown by the dotted line as a reference. Figure 12 presents a summary of variation in the energy fluxes as the Reynolds number increases.

For $R \ll 1$, $\langle E_m \rangle$, $\langle W_m \rangle$, $\langle D_m \rangle$ are very close to the quantities calculated from the Munk solution. For $R < R_C$ the steady solution is stable thus $\langle E_e \rangle = 0$. When R exceeds R_C the steady solution becomes unstable and the eddies in the boundary layer appear. The energy of the eddy motion $\langle E_e \rangle$ grows with increasing $R - R_C$. The linear extrapolation of $\langle E_e \rangle$ (or even better $\langle D_e \rangle$) as a function of $R - R_C$ in the vicinity of R_C gives the estimate of the critical value of Reynolds number, $R_C = 0.38$. With the growth of eddy intensity for $R > R_C$ the total flux of energy from the averaged motion to the eddy motion, $\langle G \rangle$, also increases as well as the total dissipation in the eddy motion $\langle D_e \rangle$. The total dissipation in the averaged motion $\langle D_m \rangle$ decreases.

An interesting feature to note is that the kinetic energy of the mean current $\langle E_m \rangle$ stays close to $\langle E_{Munk} \rangle$ in a wide range of Reynolds numbers, $0 < R < 1.5$, not only for

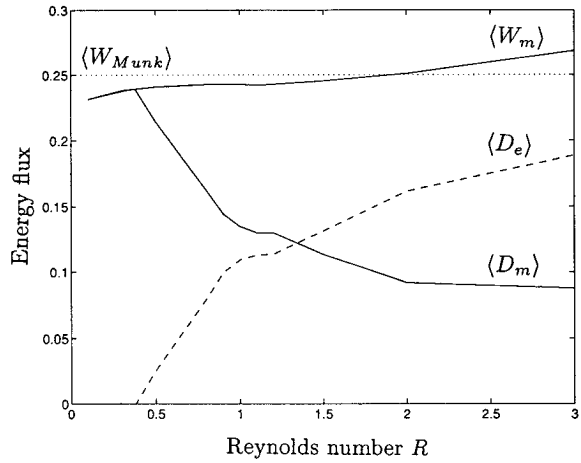

Figure 12. The variation of energy fluxes with Reynolds number R. The solid line is the dissipation of energy in the mean flow $\langle D_m \rangle$. The dashed line is the dissipation of energy by eddies $\langle D_e \rangle$. The dash-dotted line is the energy input by the wind $\langle W_m \rangle = \langle D_m \rangle + \langle D_e \rangle$. The value $\langle W_{Munk} \rangle = 0.25$ corresponding to the Munk solution is shown by the dotted line.

$R \ll 1$. $\langle E_m \rangle$ deviates from $\langle E_{Munk} \rangle$ for $R > R_L$. This is associated with the growth of the recirculation gyre and an increase of its energy.

The appearance of another regime as R exceeds R_L is also conspicuously seen in the behavior of $\langle D_m \rangle$ and $\langle D_e \rangle$. These curves have noticeable bending points near R_L.

Another feature to note is that the energy input $\langle W_m \rangle$ remains practically unchanged (Fig. 12). This holds even for $R > R_L$ when the solution of the problem differs significantly from the Munk solution and the Sverdrup interior solution is distorted by the growing recirculation gyre (Fig. 2 $R = 2, R = 3$). The increase of the recirculation gyre energy and the energy of eddies causes the substantial increase of the total kinetic energy of the system and, correspondingly, the noticeable increase of the time T_S needed for reaching the quasistationary regime

$$T_S \simeq \frac{\text{the total kinetic energy of the system}}{\text{the rate of energy input in the system per unit time}}. \tag{23}$$

The energy of the eddy motion $\langle E_e \rangle$ grows with increasing R and becomes comparable with the energy of the mean current $\langle E_m \rangle$ near $R = 1$ but as the recirculation gyre becomes prominent for $R > R_L$ their ratio becomes roughly constant (Fig. 11).

The arguments based on the analysis of the energy characteristics of the system support the idea that the breakdown of the steady solution of the boundary layer type happens at R_L.

5. Balance of vorticity

a. Integral balance of vorticity. Integrating the vorticity equation ((12) in KSPB) over the basin we have

$$\frac{d\Omega}{dt} = \gamma^3 \oint_\Gamma \frac{\partial \omega}{\partial n} d\Gamma + \int_0^1 \int_0^1 \nabla \times \tau \, dx \, dy \tag{24}$$

where Ω is the total vorticity of the basin, Γ is the boundary of our basin, and n is the outer normal. In deriving (24) we assumed that the integral effect of advection of the relative and planetary vorticity is equal to zero. Thus, the variation of Ω is caused by the external source of the vorticity and viscous diffusion of the relative vorticity across the boundary. (Recall that we consider no-slip boundary conditions at the western and eastern coasts.) In this case Ω equals the velocity circulation along the northern and southern boundaries

$$\Omega = \int_0^1 [u(x, y = 0, t) - u(x, y = 1, t)] \, dx. \tag{25}$$

For the steady linear Munk solution (8), (9), (10) $\Omega = -\pi + O(\gamma)$. When R increases the recirculation gyre grows, resulting in an increase of the velocity along the northern boundary and therefore in an increase of Ω of the time-averaged current. For example, $\overline{\Omega} = -3.28$ for $R = 0.5$; $\overline{\Omega} = -3.73$ for $R = 1$; $\overline{\Omega} = -16.7$ for $R = 2$; $\overline{\Omega} = -37.7$ for $R = 3$.

The total input of the vorticity due to the wind stress curl does not depend on t and equals $(-2/\pi)$. As follows from (24), in the steady and quasistationary regime this amount of negative vorticity should be balanced by diffusion of positive vorticity across the boundary. The peculiar character of our problem is that this diffusion takes place mainly across the western boundary of the basin where the intensive boundary current forms. It is useful to consider a y-dependence of the diffusion flux across the western boundary (Fig. 13). In the linear case, when advection of the relative vorticity is absent, the balance similar to (24) should be applicable at each y. Therefore for small Reynolds numbers we have

$$-\gamma^3 \left. \frac{\partial \omega}{\partial x} \right|_{x=0} \simeq -\int_0^1 \nabla \times \tau \, dx = \sin \pi y. \tag{26}$$

When Reynolds number R increases ($R = 0.5$; 1; 3) the eddies appearing in the western boundary current and growing recirculation gyre influence the diffusion across the western boundary (Fig. 13). In the northern half of the boundary current ($y > 0.5$) the diffusion flux for these R is oscillating around the function $\sin \pi y$, with the amplitude of this oscillations decaying for $y \to 0.5$. One of the maxima is caused by the increased eddy activity near $y = 0.7$ and another maximum near $y = 0.9$ is caused by the recirculation gyre pressing the boundary current to the western wall.

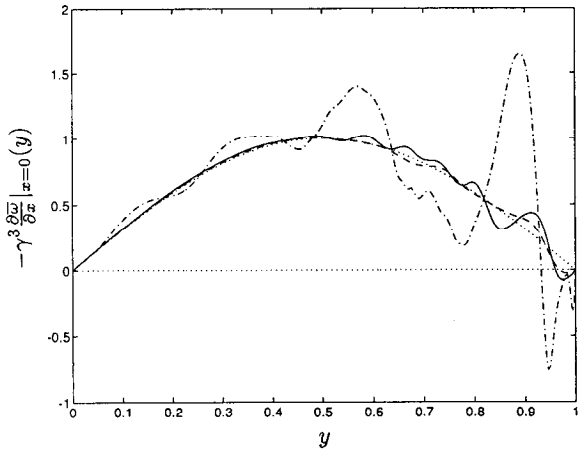

Figure 13. The diffusive flux of vorticity across the western boundary $-\gamma^3 \partial\overline{\omega}/\partial x|_{x=0}(y)$ as a function of latitude y for the time-averaged solution: $R = 0.5$ dashed line; $R = 1$ solid line; $R = 3$ dash-dotted line. The dotted line shows the flux for the Munk solution, $\sin \pi y$.

No significant departures from $\sin \pi y$ dependence are seen in the southern half of the boundary current ($y < 0.5$).

However, the total diffusion flux of the relative vorticity across the western boundary is nearly constant for all R considered ($R < 3$). Indeed, calculating the diffusion flux of relative vorticity across the northern boundary, we see that it is substantially smaller as compared to the corresponding flux across the western boundary (Fig. 14). The corresponding fluxes across the southern and eastern

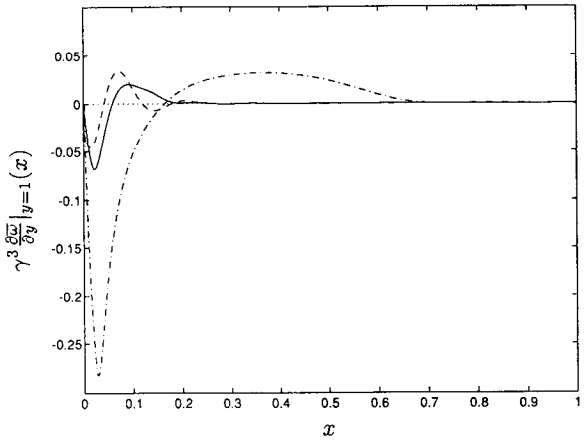

Figure 14. The diffusive flux of vorticity across the northern boundary $\gamma^3(\partial\overline{\omega}/\partial y)|_{y=1}(x)$ for the time-averaged solution: $R = 0.5$ dashed line; $R = 1$ solid line; $R = 3$ dash-dotted line.

boundaries can evidently be ignored. Thus, we have

$$-\int_0^1 \gamma^3 \frac{\partial \overline{\omega}}{\partial x} dy \simeq \frac{2}{\pi}. \tag{27}$$

b. Vorticity balance within a closed streamline. In the preceding subsection we considered the vorticity balance for the whole basin. In view of the impermeability condition at the boundary the integral effect of nonlinear terms is equal to zero. However, nonlinear terms transfer vorticity from one region to another and therefore play an important role in the local dynamics. This transfer is accomplished by both averaged and pulsation motions. The effect of advection by averaged currents can be excluded if one considers the vorticity balance in the region enclosed by an isoline of the averaged stream function. Indeed, if we average the vorticity equation ((12) from KSPB) in time and then integrate it over such a region we obtain after simple transformations

$$-\iint_{\overline{\psi}} \epsilon^2 \overline{J(\psi', \omega')}\, dx\, dy + \gamma^3 \oint_{\overline{\psi}} \frac{\partial \overline{\omega}}{\partial n} ds + \iint_{\overline{\psi}} \nabla \times \tau\, dx\, dy = 0 \tag{28}$$

or

$$\overline{\Omega}_{\text{eddies}}(\overline{\psi}) + \overline{\Omega}_{\text{visc}}(\overline{\psi}) + \overline{\Omega}_{\text{wind}}(\overline{\psi}) = 0 \tag{29}$$

where n is the outer normal to the contour $\overline{\psi} = const.$ Note the appearance of a term on the left-hand side of (28) that describes the divergence of the vorticity flux owing to eddies (pulsations).

Figure 15 shows different terms in (28) as a function of $\overline{\psi}$, a magnitude of $\overline{\psi}$-isoline enclosing the region. For better seeing the relative importance of the terms in a whole range of $\overline{\psi}$ we divided all the terms by the area A of the region enclosed by $\overline{\psi} = const.$ In addition to these three curves, A as a function of $\overline{\psi}$ is also present in Figure 15. In the case when $\overline{\psi} = 0$, this isoline coincides with the basin boundary and $A(0) = 1$, $\overline{\Omega}_{\text{eddies}}(0) = 0$. The vorticity balance in this case was considered in the preceding subsection. It should be stressed again that the vorticity transfer across the boundary in this case is accomplished by diffusion only. In view of the impermeability condition, the vorticity transfer across the boundary of the basin, caused by pulsations, equals zero.

For small $R < R_C$, when the steady solution establishes, there are no pulsations. That is why for any closed $\overline{\psi}$-isoline the balance between the wind stress input and the effect of diffusion takes place: $\overline{\Omega}_{\text{visc}}(\overline{\psi}) + \overline{\Omega}_{\text{wind}}(\overline{\psi}) = 0$.

When the Reynolds number increases (accordingly the coefficient of viscosity decreases) the integral effect of the viscous diffusion of positive vorticity into the interior of the basin decreases. Therefore, in the quasistationary regime the effect of pulsations in transferring the vorticity becomes noticeable. For example, for $R = 2$

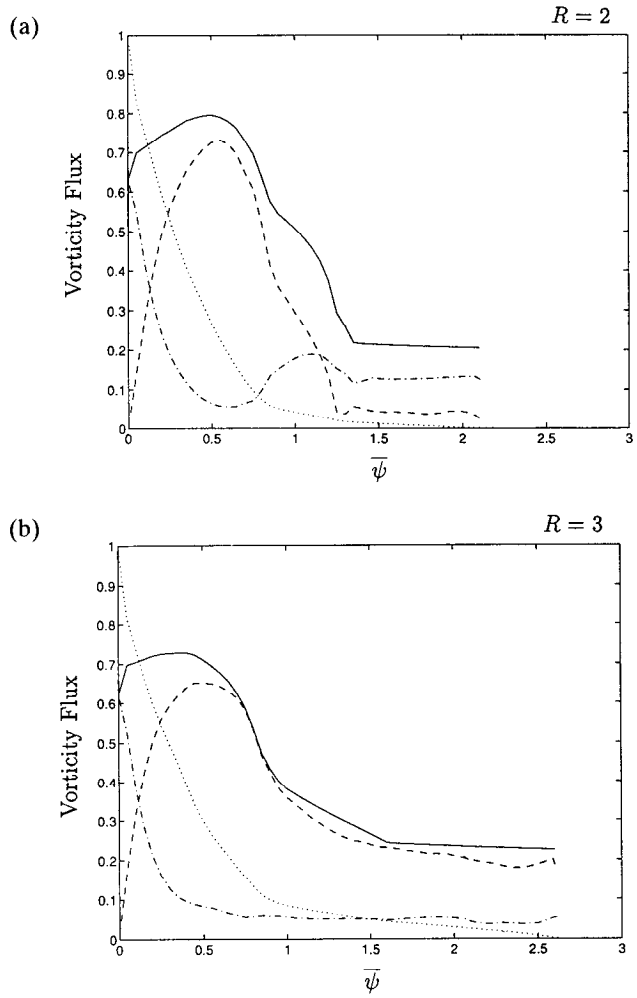

Figure 15. The terms in the averaged vorticity equation (29) as functions of the magnitude of the time-averaged stream function $\overline{\psi}$ in the experiments with (a) $R = 2$; (b) $R = 3$. The dotted line is the area $A(\overline{\psi})$ enclosed by the isoline $\overline{\psi} = const.$ The solid line is the input of vorticity by the wind (with negative sign and divided by the area) $-\overline{\Omega}_{\text{wind}}(\overline{\psi})/A(\overline{\psi})$; the dashed line is the vorticity brought in by eddies $\overline{\Omega}_{\text{eddies}}(\overline{\psi})/A(\overline{\psi})$; the dash-dotted line is the diffusion of vorticity due to viscosity $\overline{\Omega}_{\text{visc}}(\overline{\psi})/A(\overline{\psi})$.

the transport of positive vorticity to the basin interior, $0.2 < \overline{\psi} < 0.8$, is performed mostly by eddies (Fig. 15).

For $\overline{\psi} > 1.2$ we have essentially the balance within the recirculation gyre. Here the area bounded by $\overline{\psi} = const$ depends approximately linear on $\overline{\psi}_{max} - \overline{\psi}$; $A \simeq r^2 \simeq (\overline{\psi}_{\text{max}} - \overline{\psi})$, r is the radius from the center of the gyre. Therefore, the contribution of the wind divided by the area $\overline{\Omega}_{\text{wind}}(\overline{\psi})/A(\overline{\psi})$ is approximately constant. For $R = 2$ the

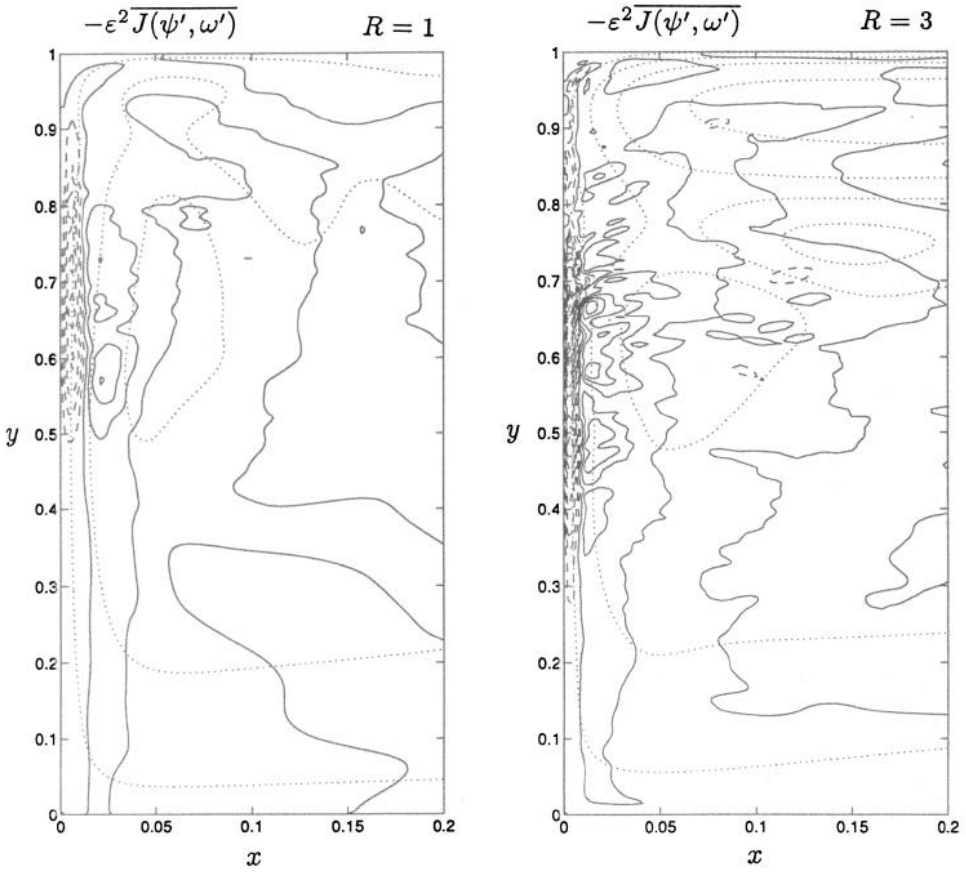

Figure 16. The spatial distribution of the divergence of the eddy vorticity flux $-\epsilon^2\overline{J(\psi', \omega')}$ in the western boundary layer for the time-averaged solution in the experiments with $R = 1$ and $R = 3$. The positive and zero isolines are shown by solid lines, the negative — by dashed ones. The contour interval, $CI = 20$. The dotted isolines show the typical time-averaged streamlines, $\overline{\psi} = 0.1; 0.5; 1; 2$.

role of viscosity, as we see, is still significant. But for $R = 3$ the balance between the negative input of the wind curl and positive vorticity brought in by eddies becomes dominant within the recirculation gyre. The explicit viscosity plays a secondary role. The dominant role of eddies results in the homogenization of potential vorticity within the gyre, which is seen in Figure 7.

It is appropriate here to consider the spatial distribution of the term $-\epsilon^2\overline{J(\psi', \omega')}$ (Fig. 16). This field is somewhat noisy because of higher order spatial derivatives involved in its evaluation, but the regions of positive and negative values can still be reliably identified. There are two extrema of this term in the northern part of the western boundary current where the maximum of eddy activity is observed. We see

the minimum near the boundary and the maximum to the east of this minimum. This indicates that the eddies in this region do intensify the transfer of positive vorticity from the near boundary region (viscous sublayer) into the inertial part of the boundary current. This is equivalent, in some sense, to increasing the "effective" viscosity which provides the feedback necessary for constraining the growth of the recirculation gyre happening in the interval of Reynolds numbers $R_C < R < R_L$ (as we have seen in Fig. 4).

We note that the typical value of $-\epsilon^2\overline{J(\psi', \omega')}$ grows from 0 for $R = R_C$ to $O(1/\epsilon)$ for $R = R_L$ and then it saturates for $R > R_L$. This indicates that the eddies in the western boundary layer become nonlinearly saturated near $R = R_L$. Since the size and velocities within eddies become independent of viscosity and the thickness of the viscous sublayer $(\epsilon/\sqrt{R})$ decreases for increasing Reynolds number, it becomes more and more difficult for these eddies to transfer the positive vorticity from the near-wall area to the inertial part of the boundary layer. As a result the significant growth of the recirculation gyre appears for $R > R_L$.

6. Recirculation gyre

Within this and the previous paper (KSPB) we repeatedly focused on the description of the recirculation gyre. In this section we collect all the basic points together to consistently discuss the process of the formation of the recirculation gyre for different Reynolds numbers R. The formation of the recirculation gyre starts at the spin-up stage already. Consider the case $R = 1$ once again when the recirculation gyre is sufficiently well pronounced in the time-dependent patterns (KSPB, Fig. 1). At the very early stage dynamics are linear and inviscid, and long Rossby waves are generated under the action of suddenly appeared wind (ibid.; Fig. 1a, b). The westward propagation of these waves leads to the formation of the time-dependent boundary layer at the western coast of the ocean. The width of this layer decreases as time proceeds. When the boundary layer becomes sufficiently narrow the role of nonlinear terms and viscosity increases and the solution ceases to be symmetric relative to $y = 0.5$ (ibid., Fig. 1c). The closed ψ-isolines in the vicinity of the west coast are stretched along the coast and instead of one maximum two maxima appear (ibid., Fig. 1d). The north maximum can be considered as an embryo of the recirculation gyre. Moving to the north it reaches the northwest corner of the basin taking this position as a permanent one (ibid., Fig. 1e). After reaching this location the gyre continues to evolve; its size and intensity are eventually determined by the balance between viscous and inertial effects. It is worth noting that the anticyclone going behind is absorbed in the northwest corner by this stalled gyre (ibid., Fig. 1f, g, h). Simultaneously a new anticyclone appears in the vicinity of $y = 0.5$ which will move northward and be absorbed by the standing gyre afterwards and so on (ibid., Fig. 1h). One can reason that the system has reached the quasistationary regime: the spin-up stage is over and the recirculation gyre has been formed.

The described picture of the formation of the recirculation gyre appeared to be typical for other Reynolds numbers also. However, as has been shown already recirculation gyres with noticeable intensities and sizes are formed at $R > R_L$ only (Fig. 1) with the time of the gyre formation depending strongly on R. It should be stressed that the eddy chain formed in the boundary layer generates the oscillation of the recirculation gyre intensity with a rather small amplitude merely (about 15%). The formation of the recirculation gyre is not caused by these eddies. In the slip case, when the chain of moving eddies is absent altogether, the formation of the recirculation gyre is still observed with stages (a)–(d) being very similar despite the difference in boundary conditions (KSPB, Fig. 1 and 3).

What physical mechanism is responsible for the formation of the recirculation gyre? For finite Reynolds numbers advection of the relative vorticity $\epsilon^2\omega$ plays a significant role. At the spin-up stage, diffusion of the relative vorticity is small outside the region very near to the western coast and the absolute value of the relative vorticity $\epsilon^2|\omega|$ increases when fluid particle moves northward (especially within the inertial part of the boundary layer where $q = \epsilon^2\omega + y$ is conserved by fluid particles). Meanwhile the relative vorticity in the interior Sverdrup region remains small as compared to the planetary vorticity y. Thus, to join the interior the particles moving in the boundary layer should somehow diminish the absolute value of the relative vorticity $\epsilon^2|\omega|$. That is why the particles tend to be within the boundary layer (under the action of diffusion of the relative vorticity) as long as possible causing a stretching of the closed streamlines along the coast. However a group of fluid particles exists that carry a substantial amount of the negative relative vorticity northward and for this reason cannot join the Sverdrup interior. These particles remain in the northwest corner of the region forming an embryo of the recirculation gyre. However the eddies in the boundary layer still play some role in the formation of the recirculation gyre. We recall that for $R < R_L$ these eddies enhance the flux of positive vorticity from the western coast while for $R > R_L$ the eddy flux of vorticity saturates. Thus the amount of the particles forming the recirculation gyre has to be substantially increased when R exceeds the critical value R_L.

What is the evolution of the embryo of the recirculation gyre? We note only that the dynamics of the gyre with closed trajectories of the fluid particles and negligibly small diffusion of the relative vorticity is rather peculiar. What will be a limit state of this evolution? We will try to crudely estimate a dependence of the intensity and the size of the quasistationary recirculation gyre on the Reynolds number R only. To do this we will assume that in the quasistationary state the permanent influx Π of the negative relative vorticity to the gyre from the south within the inertial part of the boundary current is balanced by the diffusion of the positive relative vorticity through the western coast (neglecting in a first approximation the diffusion through the southeast boundary of the gyre and the effect of eddies). Introducing a scale L_G of the gyre and estimating the total flux of the positive relative vorticity to the gyre through the

western coast as $\gamma^3(\omega_G/L_G)L_G$ we have

$$\gamma^3\omega_G = \Pi \tag{30}$$

where ω_G is a typical value of the relative vorticity of the gyre. Taking into account that within the gyre the relative and planetary vorticity are of the same order we obtain

$$\epsilon^2\omega_G = L_G. \tag{31}$$

Combining (30) and (31) and recalling the definition of R (see (8) and (9) in KSPB) gives

$$\Psi_G \simeq R^3; \qquad L_G \simeq R \tag{32}$$

where Ψ_G is a scale of the stream function for the gyre. The estimate (32) is very crude but it gives some explanation of the growth of the intensity and size of the recirculation gyre found in our computations for increasing Reynolds number R(for $R > R_L$).

7. Summary

This paper is Part II of the suggested study of the barotropic model of the subtropical gyre. The wind stress is assumed to be steady and zonal. The boundary conditions are no-slip at the eastern and western boundaries and slip at the northern and southern boundaries. The solution is characterized by the two nondimensional parameters: the width of the inertial boundary layer ϵ and the Reynolds number for the boundary current R.

A series of numerical experiments with fixed $\epsilon = 0.01$ (typical for the subtropical gyre in the ocean) and varying R have been carried out. In Part I of the study (KSPB) the two critical Reynolds numbers $R_C = 0.38$ and $R_L = 1.6$ were identified. For $R > R_C$ the time-dependent solution does not stabilize as time proceeds, and the steady solution appears to be unstable. For $R > R_L$ the breakdown of the boundary layer happens (the steady solution of the boundary layer type ceases to exist).

In this paper we have carefully analyzed the time-averaged fields of various motion characteristics, properties of the eddies, energy and vorticity balances in order to study different regimes of the motion for a broad range of Reynolds numbers.

For $R < R_C$ the viscous effects are dominant and the solution is close to the linear Munk solution. When R exceeds R_C the eddies in the western boundary layer appear due to the instability of the steady motion. These eddies cause a broadening of the northern part of the boundary layer and enhance the transfer of positive vorticity from the western boundary, that is equivalent to incorporating the increased effective viscosity in the system. Therefore in the interval $R_C < R < R_L$ the patterns of the time-averaged circulation do not significantly change.

The value of the Reynolds number R_L marks the appearance of another regime in the behavior of solution. For $R > R_L$ the dynamics of the western boundary layer becomes predominantly nonlinear. The eddies in the western boundary current can no longer enhance the effective viscosity. As a result the rapid growth of the size and the intensity of the recirculation gyre in the northwest corner of the basin appear. It is worth noting that the formation of the recirculation gyre leads to a significant increase of the total transport of the boundary current.

The energetics of the motion is analyzed in detail. The variation of the total energy is considered and a certain explanation of its spectrum is suggested. To analyze the quasistationary regime of the flow, the motion is split into the sum of the time-averaged and eddy (pulsation) motions. The total energy of the eddies E_e continuously increases with increasing R for $R > R_C$, while the total energy of the time-averaged flow E_m remains close to the value determined from the linear problem E_{Munk}. However when R exceeds R_L the quantity E_m significantly increases due to the growth of the energy of the recirculation gyre. The rate of the total time-averaged energy input into the system by the wind remains practically unchanged when R is increasing. Therefore, the time needed for reaching the quasistationary regime substantially increases for large Reynolds numbers $R > R_L$.

The analysis of potential vorticity distribution and vorticity balances shows that the dynamics of the recirculation gyre is predominantly inertial in the central part of the gyre and the vicinity of the northern boundary. The recirculation gyre is formed because of the advection of the extreme amount of negative vorticity by the inertial part of the western boundary current Π. Thus a group of recirculating fluid particles appears that cannot join the Sverdrup interior, since the region is characterized by negligible magnitudes of the relative vorticity. The limit size and the intensity of the recirculation gyre is determined by the balance between Π and the vorticity diffusion (for $R > R_L$). For $R_C < R < R_L$ the eddies in the western boundary layer incorporate a noticeable amount of diffusion into the system. For large $R > R_L$ the integral eddy vorticity transfer in the recirculation zone becomes small and the homogenization of potential vorticity within the recirculation gyre appears.

Acknowledgments. This work was launched at P .P. Shirshov Institute of Oceanology, (Moscow, Russia), continued during V. M. K. visiting Massachusetts Institute of Technology, Department of Earth, Atmospheric and Planetary Sciences (MA, USA), and Lamont-Doherty Geological Observatory of Columbia University (NY, USA) in 1990–92, during V. A. S. studying at the Scripps Institution of Oceanography (CA, USA) and again at P. P. Shirshov Institute of Oceanology during 1993–1994. Numerical computations have been carried out partly at the Scientific-Technological Center "Vector" (Moscow, Russia) and, basically, at the Scripps Institution of Oceanography under NSF grant OCE-92-1412. In 1993–1994 this paper was supported in part by the Russian Foundation for Basic Research (grants N 93-05-9263 and 94-05-17537a).

We are very thankful to many of our colleagues for discussion of the work. Our special thanks to Glenn Ierley for his very valuable comments and to two anonymous reviewers.

V. M. K. and V. A. S. are also very grateful to MIT, LDGO and SIO for their hospitality and creative atmosphere.

REFERENCES

Böning, C. W. 1986. On the influence of frictional parameterization in wind-driven ocean circulation models. Dyn. Atm. Oceans, *10,* 63–92.

Bryan, K. 1963. A numerical investigation of a nonlinear model of a wind-driven ocean. J. Atmos. Sci., *20,* 594–606.

Cessi, P. and G. R. Ierley. 1993. Nonlinear disturbances of the Western Boundary Currents. J. Phys. Oceanogr., *23,* 1727–1735.

Drazin, P. G. and W. H. Reid. 1981. Hydrodynamic Stability. Cambridge University Press, 527 pp.

Ierley, G. R. 1990. Boundary layers in the general ocean circulation. Ann. Rev. Fluid Mech., *22,* 111–42.

Ierley, G. R. and W. R. Young. 1991. Viscous instabilities in the western boundary layer. J. Phys. Oceanogr., *21,* 1323–1332.

Kamenkovich, V. M. 1966. A contribution to the theory of the inertial-viscous boundary layer in a two-dimensional model of ocean currents. Izvestiya Acad. Sci. USSR, Atm. Oceanic Phys. *2,* N12. (Translated from Russian).

—— 1977. Fundamentals of Ocean Dynamics. Elsevier Sci. Publ. Co., Amsterdam, 249 pp.

Kamenkovich, V. M., S. O. Belotserkovsky and M. S. Panteleev. 1985. On the numerical modeling of barotropic currents generated by large-scale wind field. Izvestiya Polymode, N15. P. P. Shirshov Inst. Oceanol., USSR Acad. Sci. Moscow, 3–23 (in Russian).

Kamenkovich, V. M., V. A. Sheremet, A. R. Pastushkov and S. O. Belotserkovsky. 1995. Analysis of the barotropic model of the subtropical gyre in the ocean for finite Reynolds numbers. Part I. J. Mar. Res., *53,* 959–994.

Marshall, D. and J. Marshall. 1992. Zonal penetration scale of mid-latitude oceanic jets. J. Phys. Oceanogr., *22,* 1018–1032.

Munk, W. H. 1950. On the wind-driven ocean circulation. J. Meteor. *7,* 79–93.

Sheremet, V. A., G. R. Ierley and V. K. Kamenkovich. 1996. Eigenanalysis of the two-dimensional wind-driven ocean circulation problem (in preparation).

Received: *26 November, 1994;* revised: *20 July, 1995.*